J. Fluid Mech. (2007), *vol.* 572, *pp.* 13–36.
doi:10.1017/S0022112006003235 Printed in the United Kingdom

Trailing-edge noise reduction using derivative-free optimization and large-eddy simulation

By ALISON L. MARSDEN[1], MENG WANG[2], J. E. DENNIS JR[3] AND PARVIZ MOIN[1]

[1]Mechanical Engineering Department, Stanford University, CA 94305, USA
[2]Department of Aerospace and Mechanical Engineering, University of Notre Dame, IN 46556, USA
[3]Department of Computational and Applied Mathematics, Rice University, TX 77005, USA

(Received 14 March 2006 and in revised form 10 July 2006)

Derivative-free optimization techniques are applied in conjunction with large-eddy simulation (LES) to reduce the noise generated by turbulent flow over a hydrofoil trailing edge. A cost function proportional to the radiated acoustic power is derived based on the Ffowcs Williams and Hall solution to Lighthill's equation. Optimization is performed using the surrogate-management framework with filter-based constraints for lift and drag. To make the optimization more efficient, a novel method has been developed to incorporate Reynolds-averaged Navier–Stokes (RANS) calculations for constraint evaluation. Separation of the constraint and cost-function computations using this method results in fewer expensive LES computations. This work demonstrates the ability to fully couple optimization to large-eddy simulation for time-accurate turbulent flow. The results demonstrate an 89 % reduction in noise power, which comes about primarily by the elimination of low-frequency vortex shedding. The higher-frequency broadband noise is reduced as well, by a subtle change in the lower surface near the trailing edge.

1. Introduction

The minimization of noise generated by turbulent flow over a lifting surface requires advanced simulation techniques, such as large-eddy simulation, together with non-traditional optimization methods. In this work, we develop a framework for optimizing the trailing edge of an airfoil based on a modification of the surrogate-management framework (Booker *et al.* 1999). The present work is an extension of previous work of Marsden *et al.* (2004*a*, *b*), in which shape optimization was applied to minimize vortex-shedding noise from an airfoil in laminar flow. In order to meet the challenges of the turbulent-flow problem, several issues are addressed. These include the derivation of an appropriate cost function for trailing-edge noise in turbulent flow and the development of an optimization procedure that separates constraint and cost-function evaluations in order to reduce the computation cost of the optimization.

In general, when turbulent-boundary-layer eddies are convected past the trailing edge of a body that is large (relative to the acoustic wavelength), their aeroacoustic-source characteristics are modified by the edge, resulting in a more efficient source type (Ffowcs Williams & Hall 1970; Crighton & Leppington 1971). This scattering mechanism produces strong broadband radiation to the far field, as discussed by Howe

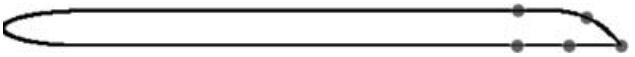

FIGURE 1. Airfoil shape with five trailing-edge control points used for deformation of the upper and lower airfoil surfaces.

(1978) and Ffowcs Williams & Hall (1970). If there is coherent vortex shedding, as is typically associated with blunt trailing edges and/or high angles of attack, then tonal or narrowband noise is also present (Brooks & Hodgson 1981; Blake & Gershfeld 1988). Additionally, it is well known that a fluctuating surface pressure may result in the excitation of structural vibrations, fatigue, and low-frequency noise radiation (Blake 1986) in a phenomenon known as singing.

Trailing-edge noise is a challenge in many aeronautical and naval applications, including hydrofoils, rotor blades, and airframe noise. In naval applications, hydrofoils that generate lift are used both for propulsion and as control surfaces. It was shown by Blake (1986) that relatively small changes in the geometry of a hydrofoil trailing edge can lead to substantial changes in the aeroacoustic performance. For example, the addition of a chamfer or knuckle to the trailing edge can significantly modify the large-scale vortex shedding in the wake, thus affecting the magnitude and spectrum of the acoustic energy generated near the trailing edge.

1.1. *Acoustic computations using large-eddy simulation*

For aeroacoustics, time-accurate computations such as large-eddy simulation (LES) are required to resolve the range of spatial and temporal flow scales relevant to noise generation. Several groups have performed trailing-edge computations which support the use of LES for accurate prediction of trailing-edge flow and noise.

Wang & Moin (2000) developed numerical prediction capabilities for trailing-edge noise based on LES and the Lighthill acoustic analogy, using the sharp(25°)-trailing-edge experiment of Blake (1975) as a test case to validate the computational methods. In this approach the acoustic field is decoupled from its hydrodynamic source field, which is computed using incompressible flow equations based on the low-Mach-number approximation. Their simulation results have established the feasibility of the LES approach for predicting the basic statistics and structure of the velocity and surface-pressure fields in the presence of unsteady separation near the trailing edge. The acoustic far field is computed using Lighthill's theory with an approximate hard-wall Green's function and following the integral formulation of Ffowcs Williams & Hall (1970). The acoustic evaluation is performed in the Fourier frequency domain. Further validation of this approach was provided by Wang (2005), who simulated a recent experiment at the University of Notre Dame (Olson & Mueller 2004) involving a more blunt (45°) trailing edge (see figure 1). Computations were carried out to determine the source-term characteristics and the far-field noise spectra.

The variational form of the Lighthill equation was used to compute the trailing-edge noise by Oberai, Roknaldin & Hughes (2002). In this work, the effect of a finite airfoil chord was studied, and the details of the trailing-edge geometry were included in the computation of the far-field noise.

1.2. *Derivative-free optimization using surrogates*

Using the computational methods of Wang & Moin (2000) and Wang (2005) as a basis, we now extend this work from noise prediction to minimization. In choosing an appropriate optimization method for the trailing-edge problem, several

challenges arise. Optimization of unsteady-flow problems, such as the trailing-edge-noise problem, is difficult using standard gradient-based methods. Although adjoint solvers provide an efficient method of computing gradients for problems with many design variables (Jameson, Martinelli & Pierce 1998), they present data-storage issues for unsteady flows and their implementation is flow-solver dependent. Additional difficulties arise with adjoint methods for constrained optimization because each constraint requires an additional adjoint equation and its solution. Derivative-free optimization methods offer a viable alternative but are often dismissed because of their computational expense.

In this work, we use a tailored and extended version of the surrogate-management framework (SMF) developed by Booker *et al.* (1999) to optimize the trailing-edge shape. The SMF method is a derivative-free method which is made highly efficient by the incorporation of surrogates. Convergence of the extended SMF method comes from mesh-adaptive direct search (Audet & Dennis 2004*a*) and incorporates surrogate functions for increased efficiency. Several recent extensions of this method have made it more suitable for the trailing-edge problem, particularly for constrained optimization.

Optimization using related methods has been performed in previous work to suppress the laminar vortex-shedding noise from an acoustically compact airfoil. A novel adaptation of the SMF method with constraints was validated for optimal aeroacoustic shape design with constraints on lift and drag by Marsden *et al.* (2004*a*, *b*). These laminar-flow cases validate the optimization technique for an unsteady fluid mechanics problem and demonstrate its robustness and computational efficiency.

1.3. *Problem formulation and outline*

We aimed to minimize the broadband noise from turbulent flow over the airfoil shown in figure 1 at a chord Reynolds number $Re = 1.9 \times 10^6$ and a Mach number $M = 0.09$. This airfoil has a bevelled 45° trailing edge with the same geometry as that of the Blake (1975) trailing edges used previously by Marsden *et al.* (2004*a*, *b*) in the laminar-flow cases. The leading edge is more aerodynamic, and the longer straight section allows for full development of the turbulent boundary layers. The airfoil has a chord-to-thickness ratio of 18, or $c = 18$ and $h = 1$ in dimensionless units (normalized by the thickness). This geometry was also used in the recent Notre Dame experiments of Olson & Mueller (2004) and the companion large-eddy simulation by Wang (2005).

The cost function for an acoustically non-compact airfoil is derived in § 2. It is based on Lighthill's theory and is proportional to the total radiated acoustic power. LES is used for source-field computations. To address the high computational cost of turbulent calculations, we introduce in § 4.1 a method to incorporate both Reynolds-averaged Navier–Stokes (RANS) and LES into the optimization procedure. This allows for determination of any constraint violation in advance using RANS, avoiding unnecessary costly LES evaluations when lift and drag constraints are violated.

The paper is structured as follows. In § 2 we outline the procedure used for acoustic computations, and we derive a cost function to measure the far-field noise. A general overview of the surrogate-management framework for constrained optimization is presented in § 3. The method is then extended for use in this problem in § 4. Application of a new polling method, developed by Audet & Dennis (2004*a*), is presented in § 5. Finally, results from optimization of the trailing edge are presented and analysed in § 6, showing as much as 89 % reduction in the far-field noise. The paper concludes with a discussion in § 7.

2. Acoustic cost function

2.1. *Cost-function formulation*

The methodology for the acoustic computations is based on Lighthill's analogy. It is desirable to use a cost function with a simple analytical form to reduce the complexity of the optimization problem. We chose to base the cost function on the integral solution to the Lighthill equation derived by Ffowcs Williams & Hall (1970). This solution relies on the use of a hard-wall Green's function for a semi-infinite half-plane, on which the normal derivative vanishes.

Formally, the use of this approximate Green's function is justified when the foil is long and thin relative to the acoustic wavelength, i.e. when $h^* < \lambda_a^* < C^*$ (the asterisk denotes a dimensional variable) or, in dimensionless form,

$$\frac{2\pi}{MC} < \omega < \frac{2\pi}{Mh},$$

where $M = U_\infty^*/C_\infty^*$ is the free-stream Mach number and ω is the angular frequency normalized by U_∞^*/h^*. In practice, the use of this approximate Green's function can be less restrictive. In the analysis of Howe (2001), the effect of a finite chord on the noise spectrum level was found to be significant when $kC < 2.5$, where $k = M\omega$ is the acoustic wavenumber, or when $\omega < 2.5/MC$. As an example, for a Mach number $M = 0.1$ and a chord length $C = 18$ this criterion gives $\omega < 1.4$. This comfortably covers the range of important frequencies, including the vortex-shedding frequency $\omega = 2.2$, for the original airfoil.

In the LES, the Lighthill stress is given by

$$\bar{T}_{ij} = \rho \bar{u}_i \bar{u}_j + \rho \tau_{ij}, \tag{1}$$

where the first term represents the nonlinear interactions among the resolved scales and the second term is the subgrid scale contribution to the resolved scales. In the trailing-edge noise computation, we computed the Lighthill stress terms using only the resolved velocity components, on the basis of the work of Wang & Moin (2000).

Using the thin half-plane Green's function, Ffowcs Williams & Hall (1970) showed that the far-field density perturbation in the frequency domain is given by the following dimensionless form:

$$\widehat{\rho_a}(\boldsymbol{x}, \omega) \approx \frac{M^{5/2} 2 \mathrm{e}^{-\mathrm{i}(\pi/4)}}{\pi^{1/2}} \sin\frac{\theta}{2} \int_V \frac{\mathrm{e}^{\mathrm{i}k|\boldsymbol{x}|}}{4\pi|\boldsymbol{x}|} \frac{(\omega \sin\phi)^{1/2}}{(2r_0)^{3/2}} \times \left\{ \left(\widehat{u_\theta^2} - \widehat{u_r^2} \right) \sin\frac{\theta_0}{2} - 2\widehat{u_r u_\theta} \cos\frac{\theta_0}{2} \right\} \mathrm{d}^3 \boldsymbol{y}, \tag{2}$$

where the circumflex denotes a temporal Fourier transform, geometric variables are defined in figure 2, and $\sin\phi = r/|\boldsymbol{x}|$. The density and velocity are normalized by their free-stream values. The above expression captures the leading-order component of the noise. The assumptions used to derive the above equation are that the viscous stress is unimportant as a noise source and that the convection, refraction, and scattering of acoustic waves can be ignored owing to the low Mach number.

Further simplification can be made to (2) following Wang & Moin (2000) if the spanwise source extent is acoustically compact when projected in the direction of propagation. This is valid for the source region contained in the computational

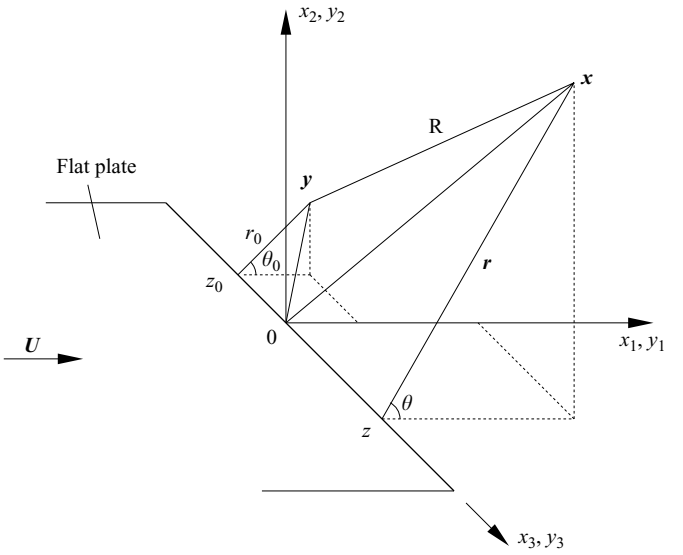

FIGURE 2. Definition of the geometric variables for the thin half-plane Green's function solution (from Wang & Moin 2000).

domain of the trailing-edge LES. With this assumption we have

$$\widehat{\rho_a}(\boldsymbol{x}, \omega) \approx \frac{M^{5/2} \mathrm{e}^{\mathrm{i}(k|\boldsymbol{x}|-\pi/4)} \omega^{1/2}}{2^{5/2}\pi^{3/2}|\boldsymbol{x}|} \sin^{1/2}\phi \sin\frac{\theta}{2}\, \widehat{S}(\omega), \tag{3}$$

where

$$\widehat{S}(\omega) = \int_V \frac{1}{r_0^{3/2}} \left\{ \left(\widehat{u_\theta^2} - \widehat{u_r^2} \right) \sin\frac{\theta_0}{2} - 2\widehat{u_r u_\theta} \cos\frac{\theta_0}{2} \right\} \mathrm{d}^3 \boldsymbol{y} \tag{4}$$

or, in physical space,

$$S(t) = \int_V \frac{1}{r_0^{3/2}} \left\{ \left(u_\theta^2 - u_r^2 \right) \sin\frac{\theta_0}{2} - 2u_r u_\theta \cos\frac{\theta_0}{2} \right\} \mathrm{d}^3 \boldsymbol{y}. \tag{5}$$

Equation (5) consists of three contributions. For convenience we will refer to the contributions of the terms containing u_r^2, u_θ^2, and $u_r u_\theta$ as S_{rr}, $S_{\theta\theta}$, and $S_{r\theta}$, respectively.

We can now define a cost function that measures the far-field noise radiated from the trailing edge. Rearranging (3), we have

$$\widehat{\rho_a}(\boldsymbol{x}, \omega) \left(\frac{|\boldsymbol{x}|}{M^{5/2} \sin\dfrac{\theta}{2} \sin^{1/2}\phi} \right) = \frac{\omega^{1/2} \widehat{S}(\omega)}{2^{5/2}\pi^{3/2}} \mathrm{e}^{\mathrm{i}(k|\boldsymbol{x}|-\pi/4)}. \tag{6}$$

Taking the magnitude of both sides leads to

$$\left\| \widehat{\rho_a}(\boldsymbol{x}, \omega) \left(\frac{|\boldsymbol{x}|}{M^{5/2} \sin\dfrac{\theta}{2} \sin^{1/2}\phi} \right) \right\| = \frac{\omega^{1/2}}{2^{5/2}\pi^{3/2}} \| \widehat{S}(\omega) \|. \tag{7}$$

Using optimization we are interested in minimizing the total radiated noise over the

entire range of frequencies. This quantity is best expressed by computing the integral of the power spectrum. Taking the square of (7) we have

$$\Phi_{\rho_a}\left(\frac{|\boldsymbol{x}|^2}{M^5\sin^2\frac{\theta}{2}\sin\phi}\right)=\frac{\omega}{2^5\pi^3}\Phi_{ss}(\omega), \tag{8}$$

where Φ_{ρ_a} is the frequency spectrum of the acoustic density and $\Phi_{ss}(\omega)$ is the spectrum of the acoustic source term. We can relate the pressure power spectrum to the density spectrum through γ, the ratio of specific heats:

$$\Phi_{p_a}=\gamma^2\Phi_{\rho_a}, \tag{9}$$

where the acoustic pressure and density are normalized by the free-stream pressure and density, respectively. We therefore define $j(\omega)$, which is directly proportional to the acoustic pressure spectrum at a given frequency ω:

$$j(\omega)\equiv\Phi_{p_a}\left(\frac{|\boldsymbol{x}|^2}{M^5\sin^2\frac{\theta}{2}\sin\phi}\right)=\frac{\gamma^2}{2^5\pi^3}\omega\Phi_{ss}(\omega). \tag{10}$$

Integrating over all frequencies, we define the cost function $J(\boldsymbol{a})$:

$$J(\boldsymbol{a})=\int j(\omega)\,\mathrm{d}\omega, \tag{11}$$

where $\boldsymbol{a}$ is the vector of the shape parameters. Using this definition, the cost function $J(\boldsymbol{a})$ is directly proportional to the total acoustic power at an arbitrary location $\boldsymbol{x}$, and can be used in the optimization to represent the noise radiated by the trailing edge.

It is worth noting here that in the case of a general airfoil shape, the use of the integral solution of Ffowcs Williams & Hall (1970) based on the half-plane Green's function may not be justified. To account accurately for aeroacoustic diffraction by the airfoil shape it would be necessary to compute the Green's function numerically. The sound power spectra, and hence the cost function for optimization, could then be defined in terms of a convolution integral of the general Green's function with Lighthill's stress terms (Goldstein 1976). Since the directivity is not known analytically, the cost function may be defined on the basis of the noise at specific far-field locations or the total radiated noise integrated over all directions.

2.2. *Computation of the cost function*

The cost function $J(\boldsymbol{a})$ derived in the previous section depends on control parameters $\boldsymbol{a}$ corresponding to the airfoil surface deformation. The five control points used in this work are shown on the trailing edge of the airfoil in figure 1. The parameter values are defined by the displacements in the vertical direction. The deformation of the lower surface is defined by the airfoil thickness relative to the upper surface, so that the constraints on the geometry are simple bounds on minimum and maximum displacement. In both cases, a Hermite spline connects all the deformation points to the trailing-edge point and the left-hand (undeformed) region to give a continuous airfoil surface.

For a given airfoil shape, a mesh is generated, LES is performed, and the cost function is evaluated using the formulation in § 2.1. The detailed LES procedure is

discussed in § 4.1. The procedure for computing the cost function from LES is as follows. The function $S(t)$ is computed directly using the LES data at intervals of four time steps. A series of values of $S(t)$ is saved so that the acoustic computation can be performed as a post-processing step.

Once a sufficiently long series of $S(t)$ values has been collected, it is divided into segments with a 50 % overlap. Each time segment contains 512 samples. The aperiodic time series are multiplied by a Hanning-window function, and discrete Fourier transforms are performed. To compensate for the energy loss due to the Hanning-window tapering, the resulting Fourier coefficients are renormalized in such a way that the resulting spectrum gives the mean-square fluctuations of the original function when integrated over all frequencies. The final spectrum $\Phi_{ss}(\omega)$ is the average of the spectra of the segments. Once the spectrum is obtained, the cost function is computed by integrating over the frequencies; see (10) and (11).

To predict accurately the noise radiation from the entire span using a partial source field included in the LES domain, the spanwise domain size is required to be larger than the coherence length of the source field in that direction. The LES domain used in Wang & Moin (2000) was shown to be adequate for predicting noise radiation over a range of frequencies. At low frequencies, however, it was found that the spanwise source coherence estimated on the basis of surface-pressure fluctuations does not decay sufficiently, owing to the small spanwise domain size. This difficulty remains in the present calculation, owing to the large expense of performing multiple simulations in the optimization. The noise calculation is limited to the source region within the computational box. However, the results should correlate well with the total noise from an airfoil of full span. Questions concerning the calculation of the total noise from full span on the basis of the partial-span noise are discussed in Wang & Moin (2000).

3. Constrained optimization using the surrogate-management framework

In this section, we introduce the derivative-free optimization method used in this work. The surrogate-management framework (SMF) was developed by Booker *et al.* (1999) to increase the efficiency of pattern-search methods for expensive problems by incorporating the use of surrogate functions. Use of the SMF method has been demonstrated in, among other works, Booker *et al.* (1999) and Serafini (1998), where the method was successfully applied to a helicopter-rotor-blade design problem with 31 design variables.

An important modification of the SMF method is the addition of constraints in a rigorous manner using a filter; constraints were added to pattern-search methods in this way by Audet & Dennis (2004*b*) and Audet *et al.* (2000). The concept of filters for constrained optimization was first introduced by Fletcher & Leyffer (2002). The use of a filter provides a sound alternative to using a penalty function, as is commonly done in conjunction with gradient-based optimization methods. Filters also give the user valuable information about trade-offs between cost-function reduction and constraint violation. Finally, an important advantage of derivative-free optimization is that the filter approach can be formulated so as not to require Lagrange-multiplier estimates.

Use of the surrogate-management framework with a filter was demonstrated for the laminar-flow trailing-edge problem by Marsden *et al.* (2004*a*, *b*) and we refer to this work for a detailed description of the optimization procedure. In this section we give a brief overview of the optimization method, and in the next section we discuss issues specific to the turbulent-flow optimization problem.

We consider the following general constrained optimization problem:

$$\text{minimize } J(\boldsymbol{x}) \quad \text{subject to } \boldsymbol{x} \in \Omega,\ C(\boldsymbol{x}) \leqslant 0. \tag{12}$$

In the above problem statement, $J : \mathbb{R}^n \to \mathbb{R}$ is the cost function and $\boldsymbol{x}$ is the vector of parameters. The constraints are given by m functions $c_i : \mathbb{R}^n \to \mathbb{R}, i = 1, 2, \ldots, m$ such that $C(\boldsymbol{x}) = (c_1(\boldsymbol{x}), \ldots, c_m(\boldsymbol{x}))^T$. The bounds on the parameter space are defined by a polyhedron in $\mathbb{R}^n$ denoted by Ω.

In the trailing-edge problem, the cost function is defined by (11). The constraints are defined to keep lift and drag at desirable levels and enforced using a filter. To construct a filter, we first define a constraint-violation function $H \geqslant 0$, where $H : \mathbb{R}^n \to \mathbb{R}^+$ is a non-negative weighted norm of constraint violations. The constraint-violation function is defined here to prevent the lift from decreasing and the drag from increasing, as follows:

$$H = \max\left(0, \frac{L^* - L}{L^*}\right) + \max\left(0, \frac{D - D^*}{D^*}\right), \tag{13}$$

where L^* is the lift coefficient of the original airfoil and D^* is the original drag coefficient.

The value of H indicates how closely the problem constraints are being met. With multiple constraints, H may be the sum of several constraint functions, with weights chosen according to relative importance. The goal of the optimization problem is to find solutions that have a small cost-function value, together with a small (or zero) value of H.

We use values of H and J to construct a filter as follows. The feasible region of the filter is defined as the set of points in (H, J)-space that exactly satisfy $H(x) = 0$. Thus, a point x is infeasible if $H(x) > 0$. An infeasible point x' is considered filtered, or dominated, if there is an infeasible point x belonging to the filter for which $H(x) \leqslant H(x')$ and $J(x) \leqslant J(x')$. A filter $\mathcal{F}$ is defined here to be the finite set of non-dominated infeasible points plus the best feasible point found so far.

Use of a filter for constrained optimization allows for the identification of a set of solutions which make up the set of best points found during the optimization rather than a single optimal shape. The filter can be viewed as sort of Pareto front showing the trade-off between obtaining a low cost-function value (the J-axis) and satisfying constraints (the H-axis). The filter divides the space of J versus H into two areas, called the unfiltered and filtered regions. Further details on the use of filters may be found in Marsden *et al.* (2004*a*).

The filter is used together with the SMF method for optimization. The SMF method is a mesh-based pattern-search algorithm: all points evaluated are restricted to lie on a mesh in the parameter space. The first step is to evaluate a set of initial data for construction of the surrogates, which are Kriging functions in the present work. The initial data is chosen using Latin-hypercube sampling; see McKay, Conover & Beckman (1979). Following evaluation of the initial data, the SMF algorithm consists of two steps, `SEARCH` and `POLL`. The `SEARCH` step provides a means for local and global exploration of the parameter space, but it is not strictly required for convergence. In the `SEARCH` step, optimization is performed on the surrogate in order to predict the location of one or more minimizing points, and the function is evaluated at these points. If a new non-dominated point is found (i.e. the filter is improved), the search is considered successful, the surrogate is updated, and another search step is performed.

If the `SEARCH` step fails to find an improved point then it is considered unsuccessful and a `POLL` step is performed. Convergence of the SMF algorithm is guaranteed by

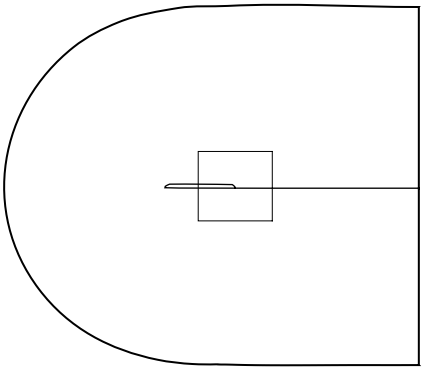

FIGURE 3. Domains used for RANS computations (thick line) and LES computations (thin line).

the POLL step, in which points neighbouring the current best point on the mesh are evaluated in a positive spanning set of directions to check whether the current best point is a mesh local optimizer. If the POLL produces an improvement in either the best feasible or least infeasible point then the next SEARCH step is performed on the current mesh. Otherwise the current best point is a local minimizer of the function on the mesh. For greater accuracy, the mesh may be refined, at which point the algorithm continues with a SEARCH step. Convergence is reached when a local minimum on the mesh is found and the mesh has been refined to the desired accuracy. Each time new data points are found in a SEARCH or POLL step, the data is added to the surrogate and it is updated.

4. Optimization procedure

4.1. *Incorporation of RANS and LES in optimization*

In extending the trailing-edge optimization from laminar to turbulent flow, the main challenge is one of increased computational cost. The cost of LES is such that it is not practically feasible to simulate the entire airfoil, and instead computations are performed in a truncated domain that includes only the trailing-edge portion of the airfoil. This makes it impossible to integrate lift and drag values over the entire airfoil surface in the LES computation. Large-eddy simulation is used to compute the cost function by integration of the acoustic source in the trailing-edge region.

The large computational cost of doing optimization using LES-based function evaluations can be mitigated by incorporating RANS into the optimization procedure. While it is not possible to obtain accurate acoustic predictions from RANS, reasonably accurate aerodynamic data, including mean lift and drag values, can be readily obtained. A steady RANS simulation of the entire airfoil requires only five single-processor SGI O3K CPU hours using the commercial package Fluent. Incompressible RANS computations are performed on a C-type mesh using the Spalart–Almaras turbulence model. Because of the orders-of-magnitude disparity in simulation time between RANS and LES, it is advantageous to use RANS calculations whenever possible and to reduce the number and size of full LES simulations.

In addition to computing lift and drag, the RANS method is used to provide boundary conditions for the LES simulation. The domains for the RANS and LES simulations are shown in figure 3. The larger domain, including the full airfoil, is used for the steady RANS simulations. Mean-velocity boundary conditions are

then interpolated from the RANS results onto the smaller rectangular LES domain. Large-eddy simulation is performed in a separate computation using the boundary conditions provided by the RANS. The smaller LES domain includes only the trailing-edge portion of the airfoil. In addition, the LES code is equipped with a turbulent-inflow generation capability employing the 'rescale and recycle' technique of Lund, Wu & Squires (1998). With this method the inflow turbulent boundary data are generated on the fly as the simulation proceeds (see Wang 2005).

Using the RANS simulation to compute lift and drag, it is possible to check the constraint-violation-function value H before starting a full LES simulation of a given airfoil shape and to avoid doing LES if the violation is too large. Decoupling the constraint computation from the cost-function computation offers a large savings in computational cost because unneeded expensive large-eddy simulations can be avoided.

In LES, a hybrid finite-difference–spectral code described in Wang & Moin (2000) is used to solve the spatially filtered time-dependent incompressible Navier–Stokes equations in generalized curvilinear coordinates. The subgrid-scale (SGS) stress tensor is modelled by the dynamic Smagorinsky model (Germano *et al.* 1991; Lilly 1992). The mesh size used in the LES computation is $1540 \times 96 \times 48$, giving a total of about 7 million mesh points. Each evaluation of the cost function using LES takes approximately 2000 single-processor hours on an IBM SP4. This allows for the removal of initial transients and a sufficiently long sampling period for statistical convergence of the acoustic spectrum and the cost-function value. The convergence of the cost function is discussed in § 6.1.

The procedure that has been implemented to incorporate LES and RANS into the optimization algorithm is outlined below. In practice, the optimization routine outputs a set of parameter values representing a unique airfoil shape. These parameter values are taken as inputs in a series of automated scripts, which then generate the airfoil geometry and the computational mesh and run the RANS and LES calculations.

The steps that are outlined below constitute a single function evaluation in the optimization algorithm. A RANS simulation is required to evaluate the constraint violation as part of every function evaluation. Depending on the constraint-violation-function value, an LES computation may or may not be performed to determine the cost-function value for a given airfoil shape. The steps in computing the cost function and constraint violation function are summarized as follows.

1. The shape parameters are used to define the airfoil geometry and corresponding trailing-edge surface mesh. A C-mesh is generated for the RANS computation (using every other trailing-edge surface point), and a truncated domain mesh is generated for the LES computation.

2. A steady RANS computation is performed using the Spalart–Allmaras turbulence model to obtain the coefficients of lift and drag.

3. The constraint-violation function H, (13), is computed using RANS lift and drag data to determine whether $H \leqslant H_{max}$, the maximum allowable value.

4. If $H \leqslant H_{max}$, the constraint violation is within the acceptable limit and the point can be included in the filter. Then the optimization may proceed to steps 5, 6, and 7. Else, if $H > H_{max}$ LES is not then performed. The point is rejected and the value of J for this shape is set to infinity.

5. Mean-velocity boundary conditions are interpolated from the RANS solution onto the boundary of the LES domain (figure 3).

6. LES is performed using interpolated boundary conditions from RANS plus turbulent-boundary-layer generation as input. The volume integral of (5) is evaluated to obtain the acoustic source.

7. The integral of the acoustic spectrum, equal to the cost-function value J, is computed in a post-processing step following the procedure in § 2.

Since the cost function and the constraint-violation function are computed separately, it is possible to use a filter with a very small value of H_{max} and so avoid doing an expensive LES simulation if H falls outside the region included in the filter. In the laminar trailing-edge problem, the filter proved to be extremely valuable in identifying a range of possible solutions, and it was shown that a large reduction in cost function could be achieved with only a small constraint violation. On the basis of the results in the laminar case, we chose a value of H_{max} that is small enough to exclude large constraint violations but large enough to identify shapes that may offer significant further cost-function reduction.

Using the above method, there are many fewer points where the cost-function value J is known (from LES) than points where H is known (from RANS). We therefore constructed one surrogate to approximate J and another to approximate H. In this way, the surrogate for the constraint function values H can incorporate all solutions found by RANS, even if $H > H_{max}$ and no corresponding J value was computed for that point. To search the parameter space, the surrogates can be summed with a penalty as follows:

$$\hat{J} = J + \alpha H, \tag{14}$$

where α is a parameter that is systematically updated using the filter at each iteration. This is a slight change from the laminar case presented in Marsden *et al.* (2004*a*), in which a single surrogate was constructed to approximate $\hat{J}$.

The large cost of turbulent-flow simulations makes parallelization of the optimization even more crucial than in the laminar-flow case. During any `SEARCH` or `POLL` step, several points are evaluated in parallel using RANS and LES. Given the large cost of a single LES solution, if it were not possible to evaluate several trailing-edge shapes simultaneously, this problem would quickly become intractable.

In the above formulation, we allow for the rejection of points that do not satisfy the constraint-violation requirement. Formally, the rejection of infeasible points is allowed within the convergence theory because of a new polling method which has been implemented for the turbulent case. Mesh-adaptive direct search (MADS) was developed by Audet & Dennis (2004*a*), and it offers several advantages over the pattern-search polling that was used in the laminar case. This new polling method is discussed in the following section.

5. Mesh-adaptive direct search

Mesh-adaptive direct search (Audet & Dennis 2004*a*) is a new method for choosing poll directions that offers greater flexibility than generalized-pattern search (GPS) polling and is capable of generating a dense set of directions. To have a dense set of polling directions means that as the mesh becomes infinitely fine, the number of possible poll directions approaches infinity. The possibility of generating a dense set of poll directions makes for a much stronger convergence theory, especially with regard to nonlinear constraints. We refer the reader to Audet & Dennis (2004*a*) for more details and a proof of convergence.

The main idea behind MADS is the introduction of a frame-size parameter that evolves separately from the mesh size. In addition to the mesh-size parameter Δ_k^m, a poll-size parameter Δ_k^p is introduced. The poll-size parameter is used to define a frame around the poll centre which contains all points that may be used to define a poll

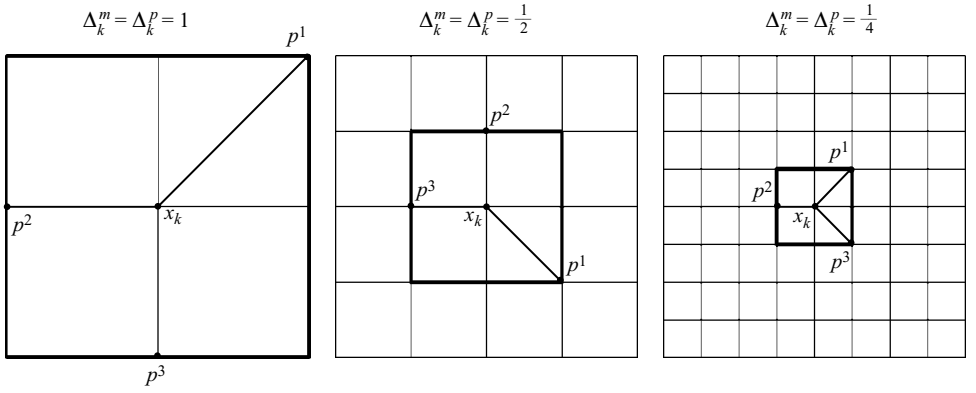

FIGURE 4. Example of GPS frames $P_k = \{x_k + \Delta_k^m d : d \in D_k\} = \{p^1, p^2, p^3\}$ for different values of $\Delta_k^m = \Delta_k^p$. In all three figures, the mesh M_k is formed by the intersections of all lines.

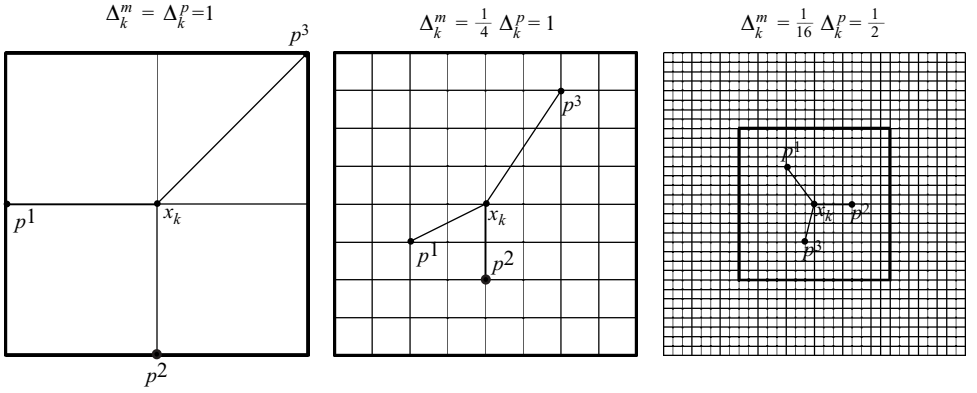

FIGURE 5. Examples of MADS polling.

direction. Figures 4 and 5 illustrate the difference between GPS and MADS polling. Figure 4 shows a sequence of successively finer meshes, and corresponding GPS poll sets in two dimensions. In the case of GPS polling, the number of points contained in the frame (the bold-outline box) remains constant (it is nine in this example) as the mesh is refined. In contrast, figure 5 shows a sequence of three successively finer meshes used for MADS polling. As the mesh is refined, each time by a factor 1/4, the frame size shrinks more slowly, so that with each refinement the frame contains more points that can be used to define a poll direction. With this illustration, we see that the number of possible poll directions increases as the mesh is refined.

Even without refining the mesh, MADS offers an advantage over GPS when $\Delta_k^m < 1$ by allowing for a larger number of directions to be represented. By performing a series of `POLL` steps, a more complete local search of the parameter space around the poll centre results. Additionally, the fact that MADS can generate a dense set of poll directions means that it will automatically conform to the boundary of the parameter space when polling on or near the boundary. Polling near the boundary of the domain therefore requires only $n + 1$ poll points.

The MADS method also offers advantages in convergence for constrained optimization. In a nonlinearly constrained optimization problem, the boundary shape

of the feasible region is unknown. Because GPS polling is limited to a finite set of directions, it is not guaranteed that the polling directions will conform to the boundary, and a step may miss the descent direction unless conforming directions are added. In contrast, MADS polling guarantees that a poll point will eventually land in the descent direction because the poll directions will fill the space as the number of mesh refinements approaches infinity. This difference makes it possible to use the barrier approach to constraints together with MADS polling, in which the cost-function value is simply set to infinity if constraints are violated.

There is a trade-off between using a filter or barrier approach for constraints in the trailing-edge problem. On the one hand, using a barrier approach would result in fewer expensive LES simulations because LES would never be performed when lift and drag constraints were violated. On the other hand, a filter allows for identification of solutions with a very small constraint violation, which may result in large cost-function reductions. An attractive middle ground is to use a filter with a small value of H_{max}, as in the present work.

6. Results

In this section we present results for turbulent-flow shape optimization using the methods described in the preceding sections. We begin by discussing the convergence of the cost function in turbulent flow. We then evaluate two optimal shapes found in the laminar-flow case (in Marsden *et al.* 2004*b*) to determine whether they also reduce noise in turbulent flow. It was found that only one of the two shapes results in noise reduction in turbulent flow. These shapes are then used as a starting point for the turbulent-flow optimization. Finally, results using the extended SMF method in fully turbulent flow are shown to result in significant noise reduction. In the turbulent-flow case, we optimize both sides of the trailing edge using five shape parameters. The geometry and control points for optimization are shown in figure 1.

6.1. *Cost-function convergence*

Since the cost-function value is used as the baseline of comparison for the optimization, we study the convergence and sensitivity of the cost-function value for the original shape before proceeding with the optimization. The spectrum $j(\omega)$ for the original airfoil was calculated using three different values of the sampling-window size, $n = 256, 512, 1024$. The cost function J, as defined in § 2, is the integral of $j(\omega)$.

It was found that a sample size $n = 256$ was not sufficient to capture the peak shedding frequency; however, this was captured by the two larger sample sizes. The cost-function values using these three window sizes differed from each other by no more than 5 %. The largest window size, $n = 1024$, did the best job of capturing the peak shedding frequency but required significantly more samples to converge the low-frequency range of the spectrum. A window size of 512 was therefore chosen since it was able to capture all frequencies of interest and the low-frequency range converged with a reasonable number of samples. Using this window size, the peak shedding frequency ω was approximately 2.2.

Figure 6 shows the time history of the three terms in the acoustic source, S_{rr} (top line), $S_{\theta\theta}$ (middle line) and $S_{r\theta}$ (bottom line), from (5), starting the simulation from $t = 0$. We see an initial period of transience, before the flow reaches a statistically steady state at around $t = 50$. Starting at this point, samples are collected for the cost-function computation until the cost-function value converges after two to three

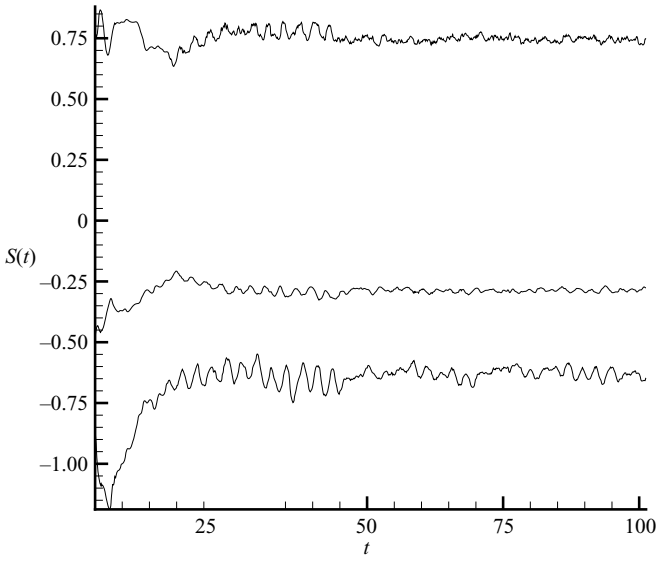

FIGURE 6. Time history of the three components of the acoustic source, S_{rr} (top line), $S_{\theta\theta}$ (middle line) and $S_{r\theta}$ (bottom line). The computation starts from time $t = 0$. The collection of samples for cost-function computation starts at $t \approx 50$ after the initial transients have been washed out. One flow-through time is approximately 20 non-dimensional time units.

		Noise	Lift	Drag
Best feasible point	laminar flow	−48 %	+229 %	−4 %
	turbulent flow	−39 %	+25 %	−16 %
Least infeasible point	laminar flow	−70 %	+262 %	+1.5 %
	turbulent flow	+18 %	+78 %	+6.6 %

TABLE 1. Cost-function, lift and drag results for two shapes in laminar and turbulent flow. These shapes were previously found to be optimal for laminar-flow noise reduction with lift and drag constraints.

flow-through times. One flow-through time across the computational domain consists of approximately 20 non-dimensional time units.

6.2. *Comparison of laminar and turbulent solutions*

In a previous work of Marsden *et al.* (2004*b*), optimal shapes were identified for the suppression of vortex-shedding noise in laminar flow. In particular, two optimal shapes, the best feasible and least infeasible, were identified when both sides of the trailing edge were deformed with constraints. In this section, we study the noise generated by these two shapes in turbulent flow to determine the correlation, if any, between shapes that reduce noise in laminar or turbulent flows. These results also serve as a starting point for optimization in turbulent flow.

A comparison of relative changes in noise, lift, and drag for the best feasible and least infeasible shapes for laminar and turbulent flows is presented in table 1. The values given in the table are relative to the original shape, and they show that changes in lift and drag have the same sign (although different magnitudes) for both shapes under consideration. Noise levels have decreased in both laminar and turbulent flow

FIGURE 7. Instantaneous streamwise-velocity contours for original (top), laminar best feasible (centre), and laminar least infeasible (bottom) shapes in turbulent flow. The best feasible shape eliminates vortex shedding in comparison with the original. Maximum velocity 1.36, minimum velocity −0.60, 15 contour levels.

for the best feasible shape, and the constraints are satisfied in both cases. As shown in the table, the best feasible shape resulted in a cost-function decrease of 48 % in laminar flow and 39 % in turbulent flow. In contrast, the least infeasible shape from the laminar-flow case caused an 18 % increase in noise level in turbulent flow, whereas the same shape had resulted in a 70 % decrease in the laminar-flow case. The constraints for this shape in turbulent flow are not satisfied, as the drag has increased by about 7 %.

Streamwise-velocity contours in turbulent flow for the original shape and for the laminar best feasible and least infeasible shapes are shown in figure 7. The original shape (shown at the top) produces large-scale vortex shedding together with smaller-scale fluctuations. We observe that the shedding has been suppressed in the middle plot, corresponding to the laminar best feasible shape. As a result, the wake is thinner. The suppression of vortex shedding is consistent with the reduction of noise. The lowest plot in the figure shows velocity contours for the laminar least infeasible shape. We observe that the thickness of the wake is decreased, but there are still significantly large vortical structures in the near-wake region. In laminar flow, the noise suppression for this shape is due to a rearrangement of vortex shedding which causes a cancellation of unsteady forces induced by the shedding of vortex pairs. In turbulent flow, this mechanism does not appear to be present and the presence of smaller-scale flow structures contributes significantly to the overall noise.

The corresponding acoustic power spectra $j(\omega)$ are shown in figure 8; the original shape is shown by the solid line, the laminar best feasible shape by the dashed line, and the laminar least infeasible shape by the dash-dot line. The acoustic cost function measures the integral of the curves shown over all frequencies. Compared with the original, the area under the curve has decreased for the best feasible shape but has increased for the least infeasible shape.

We observe in figure 8 a decrease in spectral level at low frequencies because of the elimination of vortex shedding for the best feasible shape. For the same case, we also observe a decrease in the higher-frequency noise. There is a slight increase

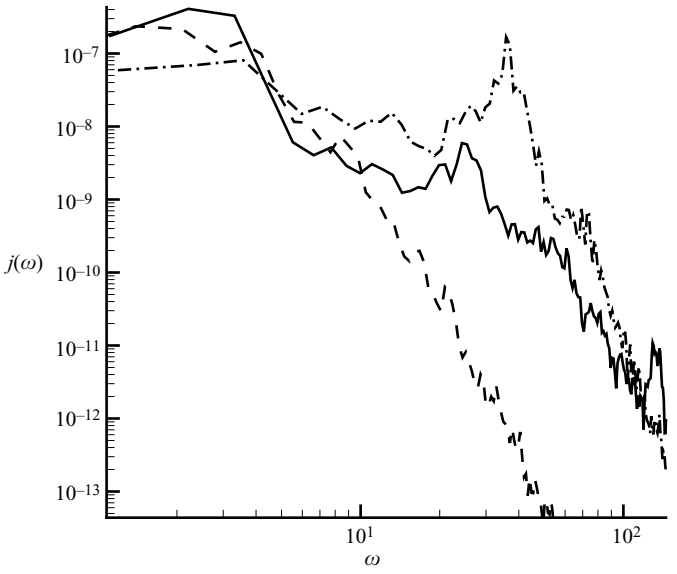

FIGURE 8. Noise spectra for original (—), laminar least infeasible (- · -), and laminar best feasible (- - -) shapes in turbulent flow. The cost function (the integral over all frequencies) has decreased for the best feasible case compared with the original but has increased for the least infeasible case.

in spectral level in the mid-range of frequencies compared with the original. These results correspond to the reduction in cost function of 39 % for this case.

In the spectrum for the least infeasible shape, we observe a significant decrease in the vortex-shedding peak. However, we also observe an increase in spectral level in the midrange and higher frequencies. In particular there is a significantly stronger secondary peak caused by a more intense shear layer emanating from the lower-surface boundary layer (see figure 7). The overall result is an increase in total acoustic power of 18 % for this case compared with the original shape.

On the basis of these results, we conclude that (not surprisingly) a shape which reduces noise in laminar flow will not necessarily reduce noise in turbulent flow and may even increase it. An optimization in laminar flow cannot be used to predict noise reduction in turbulent flow. However, there does seem to be a correlation between the reduction in large-scale vortex shedding in laminar and in turbulent flow. It seems likely that a shape which reduces large-scale shedding in laminar flow will also do so in turbulent flow. These results suggest that a laminar-flow optimization may be a useful starting point for turbulent-flow optimization if removing the vortex-shedding noise is the main objective, especially when accounting for the difference in computational cost between laminar- and turbulent-flow simulations.

6.3. *Optimal shapes for turbulent flow*

The tools described in the preceding sections may be combined to optimize the trailing-edge shape in fully turbulent flow. We use the extended SMF method for optimization with MADS polling and filter-based constraints. This procedure is adapted for turbulent flow by incorporating both RANS and LES to separate constraint and cost-function evaluations. On the basis of the results of the previous section, we include the laminar-flow shapes in the initial data set as a starting point

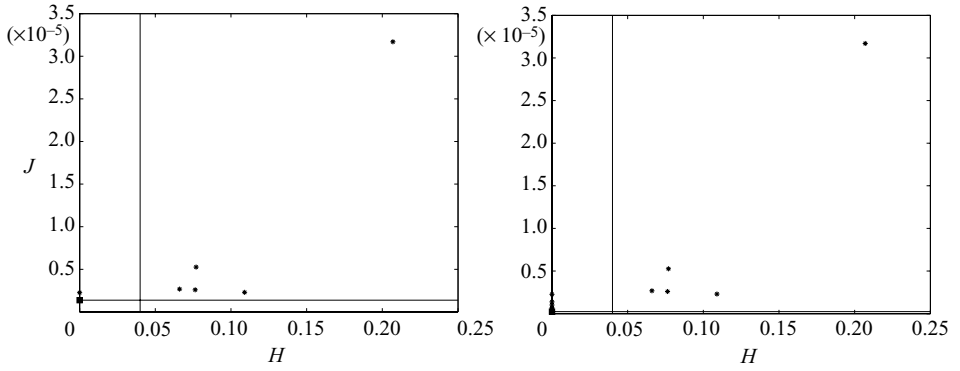

FIGURE 9. Initial filter (left) and filter after the third iteration (right) for turbulent-flow optimization. The cost function J is plotted vs. the constraint-violation function H. The solid vertical line shows the cutoff for $H \leqslant H_{max}$.

for turbulent-flow optimization. The final result is an optimal shape that reduces trailing-edge noise power by 89 % and satisfies lift and drag constraints.

The initial data set for optimization with the SMF method consisted of the same 15 points used in the laminar-flow cases, found with Latin-hypercube sampling. In addition, the two optimal shapes (best feasible and least infeasible) from the laminar-flow case were included in the initial data set, for a total of 17 initial shapes. Constraint-violation values H were found for each shape in the initial data set using RANS. Although none of the initial 15 data points satisfied the constraint criterion $H \leqslant H_{max}$, the points with the four lowest values of H plus the two laminar-flow shapes were chosen to build an initial surrogate for the cost function. All points were included in the initial surrogate for the constraints.

The initial data showed that none of the four initial shapes evaluated with the LES resulted in a reduced cost function. In contrast, in the laminar-flow optimization, two of the same shapes produced a significant reduction in cost function. The only shape that produced a reduction in turbulent flow before the first iteration was the best feasible shape from laminar flow.

The filter for the turbulent optimization problem was constructed with a maximum constraint-violation value $H_{max} = 0.04$, where H is defined as in the laminar-flow case by (13). The value of H_{max} was chosen to avoid unnecessary cost-function evaluations using LES while still allowing for shapes which may have a slight constraint violation but a low cost-function value.

The initial filter, including all the initial data, the original shape, and the two laminar-flow solutions, is shown on the left-hand side of figure 9. The solid vertical line marks the cutoff for $H \leqslant H_{max}$. Initially, there are two feasible points shown on the $H = 0$ axis. The feasible point shown by the star corresponds to the original shape. There is one feasible point in the filter in addition to the original shape, which is marked by the square, and this point corresponds to the best feasible shape from the laminar-flow case.

At the start of the optimization, the initial MADS mesh-size parameter was chosen to be 1/4 since the computational cost prohibited us from doing more than one mesh refinement. Starting MADS using a mesh-size parameter equal to unity would be equivalent to GPS in the first iteration, and MADS would not offer any advantages over GPS polling until the mesh is refined.

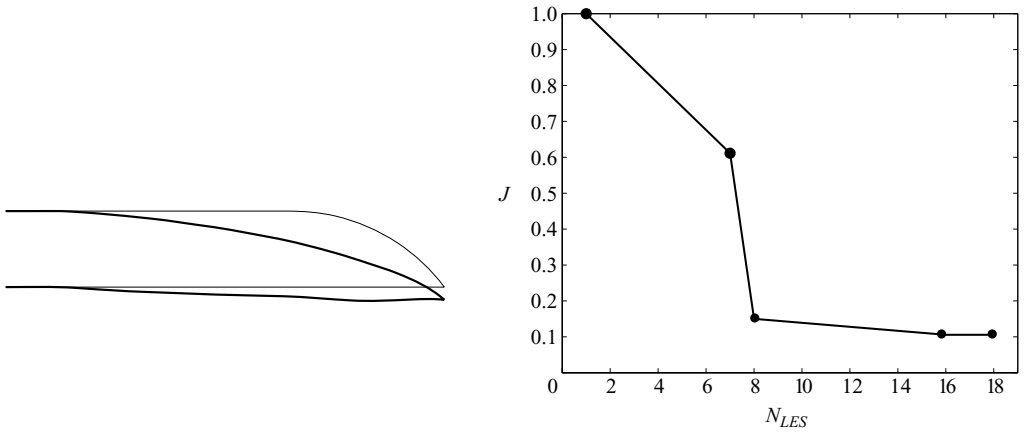

FIGURE 10. On the left: the original shape (thin line) and the best feasible shape (thick line) for turbulent-flow optimization. The best feasible shape results in an 89 % reduction in total acoustic power. The corresponding spectra are shown in figure 12. On the right: the normalized cost function vs. the number of LES evaluations for four iterations until convergence.

Noise	Lift	Drag	RANS evaluations	LES evaluations	Iterations
−85 %	+64 %	−15 %	21	8	1
−89 %	+63 %	−16.5 %	30	16	3

TABLE 2. Optimization results for turbulent flow. The first row shows the results after the first iteration. An 89 % reduction in noise is achieved after only three iterations (shown in the second row).

After only one SEARCH step of the extended SMF method, a shape which results in 85 % noise reduction was identified by the surrogate. This shape exactly satisfies the constraints, with a lift increase of 64 % and a drag decrease of 15 % compared with the original. The number of RANS evaluations required was 21, including 15 initial points, the original shape, two laminar-flow shapes and three SEARCH points. The corresponding number of LES evaluations was eight, since only four of the 15 initial points were evaluated using LES, and only one of the SEARCH points satisfied $H \leqslant H_{max}$.

After three iterations, a shape resulting in an 89 % reduction in noise was identified. This shape may be compared with the original in figure 10. We observe that the trailing edge has moved downward slightly and that the trailing-edge angle is significantly reduced. The shapes resulting from iterations 1 and 3 are qualitatively similar. However, the shape corresponding to 89 % noise reduction has a slightly smaller downward deflection in the trailing edge and is more streamlined on the lower surface compared with the shape found in iteration 1.

Constraints for the 89 %-reduction shape are satisfied, with a lift increase of 63 % and a drag decrease of 16.5 %. The computational cost breakdown is shown in table 2 along with a summary of the cost function and constraint values at iterations 1 and 3. The total number of LES evaluations has increased to 16 by iteration three. The total number of RANS evaluations after the third iteration is 30. These results suggest that if RANS had not been incorporated into the optimization procedure, the computational cost would have been much higher. Not only would the number of LES

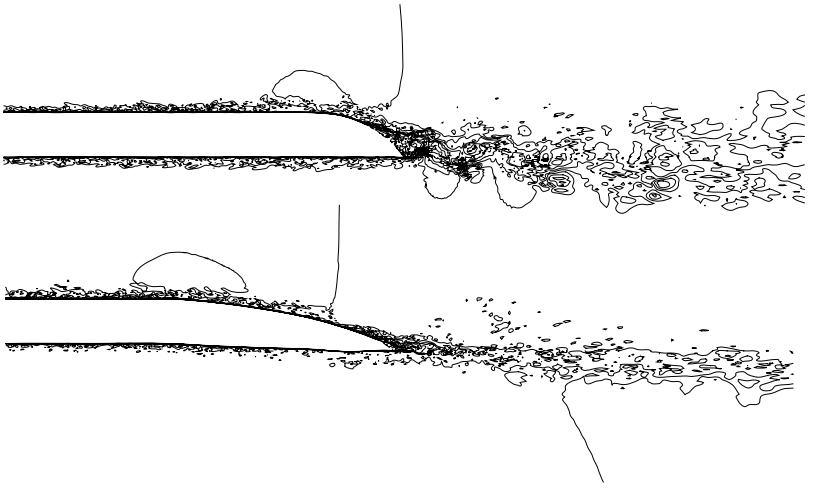

FIGURE 11. Contours of the instantaneous streamwise velocity for the original shape (top) and the best feasible shape after three iterations (bottom), which gives 89 % noise reduction. Maximum velocity 1.29, minimum velocity −0.32, 15 contour levels.

evaluations have had to nearly double but also the LES domain size would have had to include the entire airfoil to allow an evaluation of lift and drag. An additional `SEARCH` step (iteration 4) produced no further cost reduction. A plot of cost-function reduction versus the number of LES evaluations is shown on the right-hand side of figure 10.

Contours of streamwise velocity are shown for the original (top plot) and for the best feasible turbulent shape (bottom plot) after three iterations in figure 11. We observe that large-scale vortex shedding has been suppressed and that the wake thickness is reduced significantly compared with the original. The noise spectrum corresponding to this shape is shown together with the original in figure 12. The spectral level for the modified shape shows a drastic reduction at low frequencies, owing to the elimination of vortex shedding. The midrange and higher-frequency noise has also been reduced from that of the original shape.

The reduction in high-frequency noise is caused by a slight upturn of the lower surface toward the trailing edge, which results in a small adverse pressure gradient in the boundary layer. This in turn leads to a less intense shear layer emanating from the lower surface and reduced small-scale turbulence fluctuations. These observations are validated by a further examination of the flow in the trailing-edge region.

Contours of the Reynolds-stress components normal to the trailing edge, $\langle uu \rangle$, $\langle vv \rangle$, and $\langle uv \rangle$, are shown in figure 13. A comparison of results for the original shape (top plots) and optimized shape (bottom plots) shows much reduced levels of the velocity fluctuations and turbulent shear stress in both the upper and lower shear layers, largely owing to the removal of vortex shedding. These three Reynolds-stress components are directly related to the three source terms in the Ffowcs-Williams–Hall equation (see (2)–(5)). The latter are instantaneous Reynolds stresses represented in a cylindrical coordinate system. Hence, the reduction in the time-averaged Reynolds stresses demonstrated in figure 13 corresponds to a reduction in the overall acoustic-source magnitude.

Plots of pressure and the skin-friction coefficients C_p and C_f are shown on the left and right of figure 14, respectively. These data confirm the presence of a small adverse-pressure-gradient region on the pressure (lower) side near the trailing edge

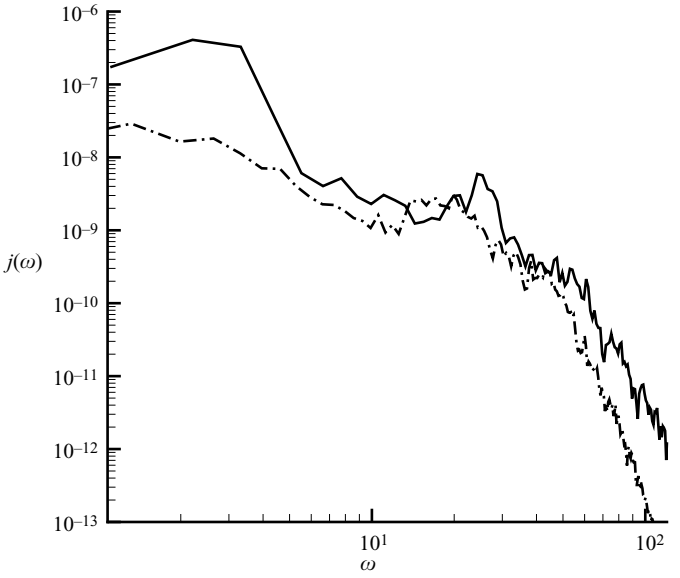

FIGURE 12. Noise spectrum for the optimized shape (– · –) and for the original shape (—) in turbulent-flow optimization. The cost function is the integral over all frequencies, and we confirm that the best feasible shape results in a significant reduction (89 %) in noise power. The corresponding trailing-edge shapes are shown in figure 11.

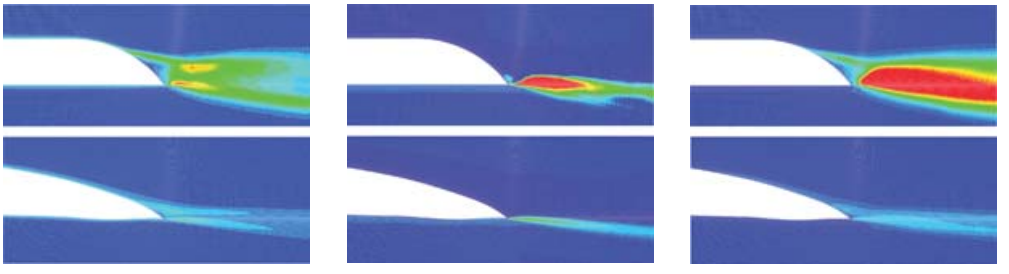

FIGURE 13. Contours of the Reynolds-stress components $\langle uu \rangle$ (left) (minimum 0, maximun 0.052, 15 levels), $\langle vv \rangle$ (center) (minimum 0, maximun 0.05, 20 levels), and $\langle uv \rangle$ (right) (minimum 0, maximun 0.015, 20 levels). Comparison of the top plots (original shape) and bottom plots (optimized shape) shows reduced velocity fluctuations and Reynolds shear stress in both the upper and lower shear layers, largely owing to the removal of vortex shedding.

for the optimized airfoil. This weakens the vorticity (i.e. lowers the C_f magnitude), thickens the boundary layer, and therefore generates less high-frequency noise. The discontinuities in C_f and in the slope of the C_p curve at about $x = -5$ are caused by the discontinuous slope of the airfoil surface, resulting from the geometry parameterization. Likewise, the four slope discontinuities on the C_f curve are due to the discontinuous second derivatives of the splines at the control points.

Pressure-side boundary-layer thickening near the trailing edge in the optimal case is also observed in the mean streamwise-velocity profiles shown in figure 15. The suction-side profiles clearly show a separated flow for the original shape, which is also obvious in the C_f plot, and an attached flow in the optimized case. Profiles in the near-wake region, in the right-hand diagram, show a narrower wake in the optimal case as compared with the original due to the absence of boundary-layer

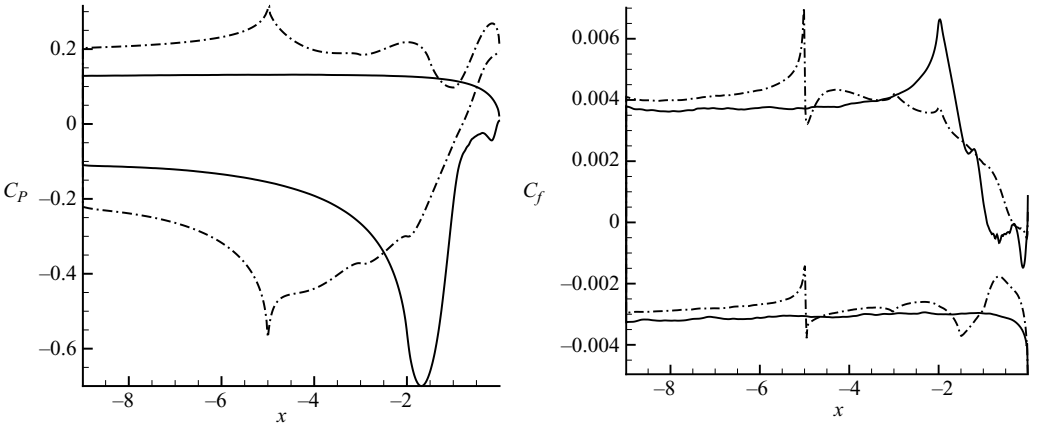

FIGURE 14. Coefficient of pressure C_p, on the left, and coefficient of friction C_f, on the right, for the original trailing-edge shape (—) and the optimized shape (— · —).

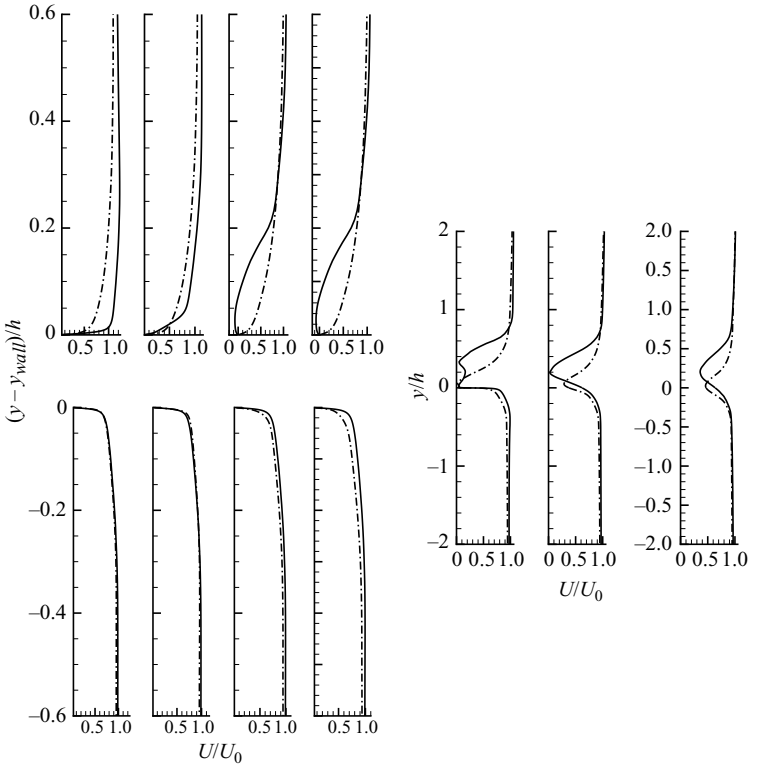

FIGURE 15. Mean streamwise-velocity profiles for the original shape (—), with vortex shedding, and for the optimized shape (— · —), without vortex shedding. Velocity profiles from the upper (suction) side and the lower (pressure) side are shown at the top and bottom of the left-hand side of the figure, respectively, at locations $x/h = -1.5, -1, -0.5$, and -0.25 from left to right. Wake profiles at locations $x/h = 0, 0.5$, and 1.0 are shown on the right side of the figure. The optimized case exhibits a narrower wake and weaker shear layers.

separation and vortex shedding. Weakening of the shear layers in the region of the trailing edge results in smaller velocity fluctuations and reduced far-field noise in the optimized case (where vortex shedding has been suppressed) as compared with the original (where there is vortex shedding).

It should be pointed out that the main objective of this work was to demonstrate conceptually that, by combining LES with the derivative-free SMF technique, we can perform difficult aeroacoustic shape design with realistic constraints at fully turbulent Reynolds numbers. An analysis of the flow field corresponding to the optimized shape confirms that the noise-generating features of the trailing-edge flow are eliminated or weakened significantly. Given the exploratory nature of this work, the problem set-up is somewhat idealized. The Blake airfoil was originally designed to study trailing-edge noise and was not meant to be quiet. Therefore the large amount of noise reduction achieved by optimization, mainly through the suppression of vortex shedding, is not surprising. If we had started from a more streamlined airfoil shape with a sharper trailing edge, the reduction might have been less drastic (that this is not always true is shown by the case of the laminar least infeasible shape in turbulent flow, shown in figures 7 and 8, which is more streamlined but noisier than the original). In a realistic application, optimization is generally performed on the entire airfoil instead of only the trailing-edge portion of the airfoil, and the angle of attack is often adjusted to maintain lift. Our approach is equally valid in this case, although such an optimization has not been performed owing to the computational expense.

7. Summary

The results of this work demonstrate the successful coupling of shape optimization to a time-accurate turbulent-flow calculation using LES. The use of novel derivative-free optimization techniques has provided a flexible optimization framework which can be applied to a wide variety of complex flow problems.

Optimization for trailing-edge noise reduction has presented several challenges which are not present in the laminar-flow case. First, a cost function needed to be defined since the airfoil is not acoustically compact for the broadband noise at all frequencies. The cost function, proportional to the radiated acoustic power, was derived on the basis of a simplified form of the Ffowcs Williams & Hall (1970) solution to the Lighthill equation, as described by Wang & Moin (2000). It involves Lighthill-stress source terms instead of compact surface dipoles.

Aside from the cost-function definition, the main challenge in the turbulent-flow optimization is one of increased computational cost. A novel method to incorporate both the LES and RANS simulations in the optimization was proposed and demonstrated. Using this method, computation of the lift and drag values was done using a RANS simulation of the entire airfoil, and the constraint violation was computed in advance of doing a full LES computation. This method results in large savings in cost by avoiding unnecessary LES evaluations in cases when constraints are violated.

The optimization method was also extended to incorporate a new polling method for the turbulent-flow case. Mesh-adaptive direct search (MADS) offers increased effectiveness and efficiency. The application of MADS to the trailing-edge problem represented its first (known to date) use in an expensive engineering application.

The analysis of a set of initial shapes in turbulent flow illustrated that shapes which reduce noise in laminar flow do not necessarily reduce noise in turbulent flow. There appears to be little correlation between noise-reducing shapes in laminar and turbulent flows. Additionally, there can be a trade-off in turbulent flow between reduction in the

high- and the low-frequency noise. However, the results do suggest that optimization in laminar flow may serve as a useful starting point for turbulent-flow optimization. Inclusion of laminar-flow solutions in the initial surrogate probably resulted in faster identification of a noise-reducing shape in turbulent flow.

In the first iteration of the extended SMF algorithm for turbulent flow, a shape that achieved an 85 % noise reduction with zero constraint violation was identified. The optimal solution produced a shape which reduced trailing-edge noise by 89 % in turbulent flow while maintaining lift and drag at desirable levels. These results validate the use of the current methods for constrained optimization, which may be applied to other complex flow problems. The acoustic spectrum showed a large decrease in low-frequency noise, because large-scale vortex shedding was suppressed, and the wake was significantly narrowed. The resulting shape is more streamlined than the original and has a smaller trailing-edge tip angle. In addition, a slight upturn of the lower surface toward the trailing edge causes a less intense shear layer and weakened higher-frequency noise.

Finally, it is interesting to contrast the main noise-reduction mechanisms observed in the laminar-flow optimization (Marsden *et al.* 2004*a*, *b*) and in the present turbulent-flow optimization. In the laminar case, the shape optimization was unable to suppress vortex shedding, and noise suppression was instead achieved through a modification of the vortex-shedding process to obtain a cancellation of unsteady forces induced by the vortices from the upper and lower shear layers. In turbulent trailing-edge flow, however, noise suppression is obtained primarily by the elimination of vortex shedding.

This work was supported by ONR under grant N00014-01-1-0423 with Ronald Joslin as program manager. Computer time was provided by the DoD's HPCMP through NRL-DC and ARL/MSRC. John Dennis was supported by the AFOSR, DOE, the IMA, the NSF, and the Ordway Endowment at the University of Minnesota. The authors also wish to thank Charles Audet and Mark Abramson for their input and helpful discussions. Part of the material in this paper was presented at the 26th Symposium on Naval Hydrodynamics, Rome, Italy, September 17–22, 2006.

REFERENCES

Audet, C., Booker, A. J., Dennis, Jr, J. E., Frank, P. D. & Moore, D. W. 2000 A surrogate-model-based method for constrained optimization. *AIAA Paper* 2000–4891.

Audet, C. & Dennis, Jr, J. E. 2004*a* Mesh adaptive direct search algorithms for constrained optimization. *Tech. Rep.* G–2004–04. Les Cahiers du GERAD, École Polytechnique de Montréal, Département de Mathématiques et de Génie Industriel, C.P. 6079, Centre-ville, Montréal (Québec), H3C 3A7 Canada.

Audet, C. & Dennis, Jr, J. E. 2004*b* A pattern search filter method for nonlinear programming without derivatives. *SIAM J. Optimization* **14** (4), 980–1010.

Blake, W. K. 1975 A statistical description of pressure and velocity fields at the trailing edge of a flat strut. *DTNSRDC Rep.* 4241. David Taylor Naval Ship R & D Center, Bethesda, Maryland.

Blake, W. K. 1986 *Mechanics of Flow-induced Sound and Vibration, Vols. I and II*. Academic.

Blake, W. K. & Gershfeld, J. L. 1988 The aeroacoustics of trailing edges. In *Frontiers in Experimental Fluid Mechanics* (ed. M. Gad-el-Hak), chap. 10. Springer.

Booker, A. J., Dennis Jr, J. E., Frank, P. D., Serafini, D. B., Torczon, V. & Trosset, M. W. 1999 A rigorous framework for optimization of expensive functions by surrogates. *Structural Optimization* **17** (1), 1–13.

Brooks, T. F. & Hodgson, T. H. 1981 Trailing edge noise prediction from measured surface pressures. *J. Sound Vib.* **78**, 69–117.

Crighton, D. G. & Leppington, F. G. 1971 On the scattering of aerodynamic noise. *J. Fluid Mech.* **46**, 557–597.

Ffowcs Williams, J. E. & Hall, L. H. 1970 Aerodynamic sound generation by turbulent flow in the vicinity of a scattering half plane. *J. Fluid Mech.* **40**, 657–670.

Fletcher, R. & Leyffer, S. 2002 Nonlinear programming without a penalty function. *Math. Programming* **91**, 239–269.

Germano, M., Piomelli, U., Moin, P. & Cabot, W. 1991 A dynamic subgrid-scale eddy-viscosity model. *Phys. Fluids* A **3**, 1760–1765.

Goldstein, M. E. 1976 *Aeroacoustics*. McGraw-Hill.

Howe, M. S. 1978 A review of the theory of trailing edge noise. *J. Sound Vib.* **61** (3), 437–465.

Howe, M. S. 2001 Edge-source acoustic Green's function for an airfoil of arbitrary chord, with application to trailing edge noise. *Q. J. Mech. Appl. Maths* **50** (1), 139–155.

Jameson, A., Martinelli, L. & Pierce, N. A. 1998 Optimum aerodynamic design using the Navier-Stokes equations. *Theoret. Comp. Fluid Dyn.* **10**, 213–237.

Lilly, D. 1992 A proposed modification of the Germano subgrid-scale closure method. *Phys. Fluids* A **4**, 633–635.

Lund, T. S., Wu, X. & Squires, K. 1998 Generation of turbulent inflow data for spatially-developing boundary layer simulations. *J. Comput. Phys.* **140**, 233–258.

Marsden, A. L., Wang, M., Dennis Jr, J. E. & Moin, P. 2004*a* Optimal aeroacoustic shape design using the surrogate management framework. *Optimization Engng* **5** (2), 235–262, Special Issue: Surrogate Optimization.

Marsden, A. L., Wang, M., Dennis Jr, J. E. & Moin, P. 2004*b* Suppression of airfoil vortex-shedding noise via derivative-free optimization. *Phys. Fluids* **16** (10), L83–L86.

McKay, M. D., Conover, W. J. & Beckman, R. J. 1979 A comparison of three methods for selecting values of input variables in the analysis of output from a computer code. *Technometrics* **21**, 239–245.

Oberai, A. A., Roknaldin, F. & Hughes, T. J. R. 2002 Computation of trailing-edge noise due to turbulent flow over an airfoil. *AIAA J.* **40** (11), 2206–2216.

Olson, S. & Mueller, T. J. 2004 An experimental study of trailing edge noise. *UNDAS-IR* 0105. Dept. of Aerospace and Mechanical Engineering, University of Notre Dame, Notre Dame, IN.

Serafini, D. B. 1998 A framework for managing models in nonlinear optimization of computationally expensive functions. PhD thesis, Rice University, Houston, TX.

Wang, M. 2005 Computation of trailing-edge aeroacoustics with vortex shedding. *Annual Research Briefs*, pp. 379–388, Center for Turbulence Research, Stanford University.

Wang, M. & Moin, P. 2000 Computation of trailing-edge flow and noise using large-eddy simulation. *AIAA J.* **38** (12), 2201–2209.